Effect of embedded metal nanocrystals on the resistive switching characteristics in NiN-based resistive random access memory cells

Min Ju Yun, Hee-Dong Kim, Seok Man Hong, Ju Hyun Park, Dong Su Jeon, and Tae Geun Kim[a)]
School of Electrical Engineering, Korea University, Seoul 136-701, South Korea

(Received 10 November 2013; accepted 23 February 2014; published online 5 March 2014)

The metal nanocrystals (NCs) embedded-NiN-based resistive random access memory cells are demonstrated using several metal NCs (i.e., Pt, Ni, and Ti) with different physical parameters in order to investigate the metal NC's dependence on resistive switching (RS) characteristics. First, depending on the electronegativity of metal, the size of metal NCs is determined and this affects the operating current of memory cells. If metal NCs with high electronegativity are incorporated, the size of the NCs is reduced; hence, the operating current is reduced owing to the reduced density of the electric field around the metal NCs. Second, the potential wells are formed by the difference of work function between the metal NCs and active layer, and the barrier height of the potential wells affects the level of operating voltage as well as the conduction mechanism of metal NCs embedded memory cells. Therefore, by understanding these correlations between the active layer and embedded metal NCs, we can optimize the RS properties of metal NCs embedded memory cells as well as predict their conduction mechanisms. © *2014 AIP Publishing LLC*.
[http://dx.doi.org/10.1063/1.4867639]

Resistive random access memory (ReRAM) has recently attracted considerable attention as a candidate for next-generation nonvolatile memory devices because of its useful properties such as a simple structure, low cost, and high-density integration. However, the use of ReRAMs also involves several issues, such as large variation in set/reset voltage (V_{SET}/V_{RESET}) and current, the operating voltage and current, and device reliability problems caused by high electric fields during its formation.[1–5] In order to overcome these problems, several methods such as multi-active layer, ion doping method, and metal embedded active layer method have been proposed.[6–8] Metal embedded methods have being actively investigated in many research groups to improve the reliability of ReRAM devices using various kinds of metal nanocrystals (NCs) (i.e., Pt, Au, Cu, Mo, Al, Co, Ni, etc.) in resistive switching (RS) materials.[8–14] Guan *et al.*[9] reported improved RS characteristics by introducing Au NCs in ZrO_2 film, which features the nondestructive readout capability and good cycling performance. Wu *et al.*[13] reported the Co embedded memory device, which have low forming voltage of −1.5 to −2.8 V and a robust negative bias unipolar resistive switching behavior with a small negative set voltage of −1.1 to −1.6 V. In addition, Ang *et al.*[14] also investigated the resistive switching and current conduction characteristics of NiO thin films embedded with Ni NCs and the influence the charging in the NC-Ni/NiO thin film has, on the current transport. However, the metal NC's dependence on RS characteristics according to the kinds of embedded metal nanocrystals in active regions has not yet been studied. Especially, when using the metal NCs embedded ReRAM, among various physical properties of metal NCs, the decisive main factors playing a crucial role in the RS have not yet been reported. Therefore, to fully understand the mechanism of metal NCs embedded ReRAM, the correlation between the active layer and embedded metal NCs should be clarified.

In our previous work,[15] we successfully demonstrated an improved memory performance in a Pt embedded-NiN-based ReRAM. As a result, we observed the reduction of set and reset variation, good endurance, and long data retention of the memory devices when the Pt embedded-NiN film was used as the RS material, compared to a conventional NiN film. In order to further understand the dependency of embedded metal NCs on the different types of metal, we have continuously studied the NiN-based ReRAM by using various embedded metal NCs.

In this work, we investigate metal NCs, such as Pt, Ni, and Ti, embedded-NiN-based memory cells and demonstrate the dependence on both RS properties and reliability for the comparative analysis according to the different types of metal. We also discuss the different switching mechanisms of the ReRAM cells depending on the work function and electronegativity of the embedded metals.

In order to prepare the samples, a Ti adhesion layer was deposited on the SiO_2/Si substrate, after which a Pt bottom electrode of 100-nm thickness was deposited by a radio frequency (RF) sputtering system. Subsequently, three multi-layers of NiN/metal-layer/NiN with thicknesses of 15/3/15 nm were deposited on the Pt/Ti/SiO_2/Si substrate using an RF sputtering system in an Ar/N_2 gas flow where the working pressure was approximately 3×10^{-3} Torr. Next, the metal NCs were formed by an annealing process in ambient N_2 gas at 650 °C for 30 s. Finally, the 100-nm Pt top electrode with a diameter of 250 μm was deposited. As shown in Fig. 1, we fabricated the Pt, Ni, and Ti

[a)]Author to whom correspondence should be addressed. Electronic mail: tgkim1@korea.ac.kr. Telephone: +82-2-924-5119. Fax: +82-2-924-5119.

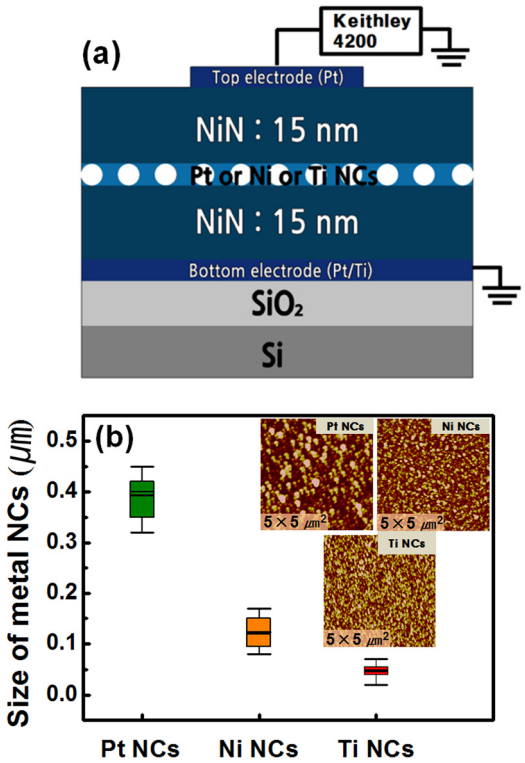

FIG. 1. (a) Schematic drawings of the metal NCs embedded memory cells and the measurement system. (b) Size distribution of the metal NC for 10 samples in each metal. The inset shows the AFM images of the Pt, Ni, and Ti NCs formed on NiN film, respectively.

embedded-NiN-based ReRAM cells, in order to examine the dependence of different types of metal. For comparison, the reference sample which is based on the conventional NiN film without embedded metal NCs is also prepared under the same process. We measured the electrical properties of memory cells using a Keithley 4200 semiconductor parameter analyzer. Fig. 1 shows the schematic drawings of the fabricated ReRAM cells and the measurement configuration.

First, in order to confirm the metal NCs, the surface roughness was observed by using an atomic force microscopy (AFM) as shown in Fig. 1(b). The AFM images show the different sizes of metal NCs depending on the different types of metal. These results are caused by the different physical properties of the metal NCs such as their electronegativity (Pt = 2.2, Ni = 1.8, and Ti = 1.5). During the annealing process, the thin metal film is transformed to the metal NCs through the process of recrystallization in metal films, and the size of NCs is determined according to the electronegativity of each metal.[16,17] Therefore, the size of NCs follows the order of Pt, Ni, and Ti as an order of electronegativity, as can be seen in the AFM images. The average size of Pt, Ni, and Ti NC is approximately 0.37 μm, 0.15 μm, and 0.15 μm, respectively, and each metal NC is formed into almost the same size in small variations under the same annealing temperature and environment. In addition, according to the size of NCs, the density of electric field focused around the metal NCs varies from metal to metal.[18] As a result, as increasing the size of metal NCs, the electric field induced around the metal NCs will be enhanced. This in turn results in the increase of operating current. In addition, the embedded metal NCs in the active layer play an important role by trapping the electrons into the potential wells, which are formed by the difference of work functions between metal NCs and their active layers. Therefore, depending on these physical properties of metal NCs such as the electronegativity and the work function, metal NCs embedded memory cells will show different RS characteristics.

In order to confirm the effect of the embedded metal NCs in the NiN-based memory cells, we investigated the RS characteristics as a function of the DC bias voltage by measuring their typical *I-V* curve characteristics, and a bipolar RS behavior is observed in all samples, as shown in Fig. 2(a). However, only the conventional memory cell without the embedded metal NCs needs an initial forming process with high voltage over 6 V for the first set operation, while the metal embedded memory cells with Pt, Ni, and Ti NCs show a forming-free operation. These results indicate that the metal NCs embedded memory cells have a low resistance in the initial state due to the focused electric field around the embedded metal NCs.

Next, the RS mechanism of metal NCs embedded memory cells was investigated; the *I-V* curves, for different

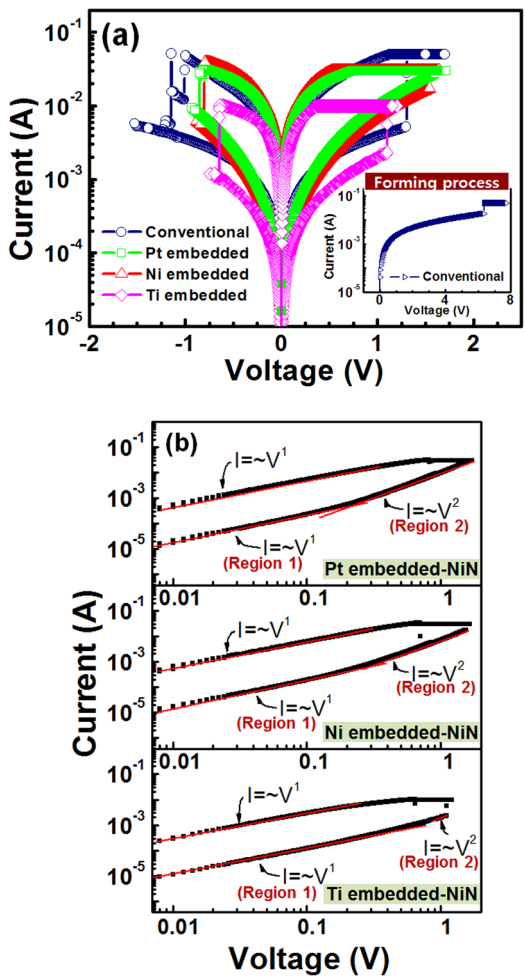

FIG. 2. (a) Typical *I-V* characteristics of both the conventional NiN-based memory cells and the metal NCs embedded memory cells. The inset shows the forming process of the conventional NiN-based ReRAM cells. (b) Linear fitting of the *I-V* curves using a log-log scale of Pt, Ni, and Ti NCs embedded memory cells, respectively.

embedded metal types have been re-plotted using a log-log scale as shown in Fig. 2(b). As shown in this figure, the slope is approximately 1 (region 1), in the entire voltage region of the low resistive state (LRS) and the low voltage region of the high resistive state (HRS), which corresponds to Ohm's law ($I \propto \sim V^1$). On the other hand, in the larger voltage region of the HRS, the current follows a square dependence on the voltage (region 2), which corresponds to Child's law ($I \propto \sim V^2$). Therefore, for all the samples of the metal NCs embedded ReRAMs, the conduction mechanism in the HRS can be explained by a space charge limited current (SCLC) theory, while the RS mechanism in the LRS can be described by a metallic filament model.[19] However, according to the different types of metal, the length of region 2 in the HRS is different for Pt, Ni, and Ti, which means that the time to fill the entire potential wells with electrons is different. This is due to the different heights of the potential wells formed by embedded metal NCs, and it depends on the difference of work function between active layers and metal NCs as shown in Fig. 3. This figure shows the schematic of the formation of electron conduction paths through the embedded metal NCs such as Pt, Ni, and Ti, respectively. As shown in this figure, according to the embedded metal types, the mechanism of electron conduction path is different because they have different types of energy band diagrams depending on the difference of work function between active layers and metal NCs. In case of the Pt and Ni NCs embedded memory cells, the work function of metal NCs is lower than the conduction band of NiN film. As a result, the potential wells are formed with a height of 1.45 eV and 0.25 eV, respectively. Therefore, when applying the bias on the top electrode, the potential wells begin to fill up with the electrons, and the conduction paths are formed after fully trapping the entire potential wells. In addition, the barrier height of the potential well determines the level of operating voltage. Compared to the Ni NCs embedded memory cells, the operating voltage of Pt NCs embedded memory cells is higher, because the barrier height of potential well is higher than Ni NCs. On the other hand, in case of the Ti NCs, the type of energy band diagram is different due to the low work function of Ti (4.9 eV). In the Ti NCs embedded-NiN films, because the metal NCs have a higher energy state than the active layer, the mechanism of the formation of electron conduction paths in the Ti NCs embedded memory cells can be explained differently with the Pt and Ni NCs. As shown in Fig. 3, in the Ti NCs embedded memory cells, the electron conduction path is formed via tunneling process of electrons via the densely formed Ti NCs. In addition, through this process, the conduction path can be formed more quickly than the Pt and Ni NCs, because it is not necessary to fill the potential wells with electrons in the Ti NCs embedded memory cells. As a result, as was mentioned before, in the *I-V* curves re-plotted using a log-log scale, the length of region 2 in the HRS is different depending on the time to form the electron conduction paths via each embedded metal NCs; Pt is longest, followed by Ni and Ti NCs as shown in Fig. 2(b). These experimental results demonstrate the conduction mechanism of each metal NCs embedded memory cells depending on the metal type.

Then, in order to examine the RS performance of the metal NCs embedded memory cells, we investigated the distributions of the set/reset voltage and current as shown in Fig. 4. Compared to the conventional memory cells, the variations of the operating voltage and current in the metal NCs embedded memory cells were reduced by the enhanced electric field effect near the metal NCs. In addition, in the operating current at $V_{READ} = 0.1$ V, we confirm the size effect of the metal NCs, which shows the increase in operating current of memory cells as the size of NCs increases. Also, as mentioned before, the set/reset voltages of the memory cells are observed to be different depending on the work function of metal NCs; the set/reset voltage and current are largest in Pt, followed by Ni and Ti, according to the work function of metal and the size of NCs, respectively.

In order to examine the reliability of metal NCs embedded memory cells, we also measured both data retention and endurance at room temperature (RT), followed by post endurance-retention and high-temperature retention at 85 °C. Figure 5 shows retention properties at RT, where conventional memory cells exhibited the obvious degradation in the LRS after 10^3 s, and the current ratio was reduced from 0.15×10^2 to 0.08×10^2 after 10^5 s. On the other hand, the Ni and Pt NCs embedded memory cells were stable in both

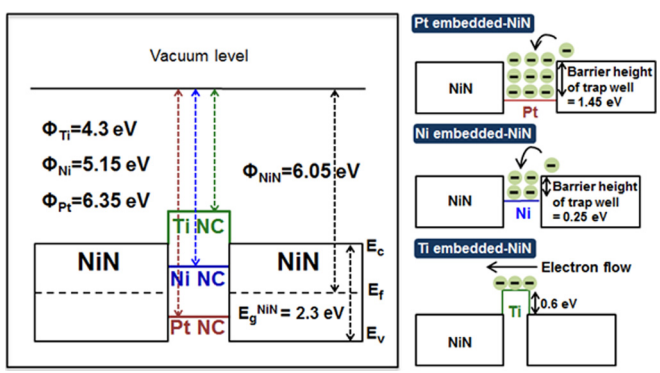

FIG. 3. Schematics of the energy diagram in the metal NCs embedded-NiN film and the mechanism for the formation of conducting path in the Pt, Ni, and Ti NCs embedded memory cells, respectively.

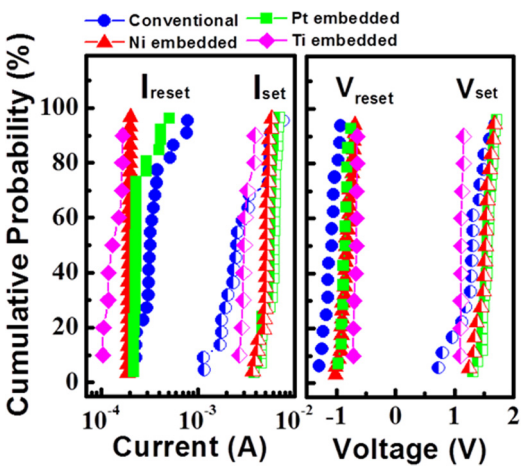

FIG. 4. Probability plots of the operating current at $V_{READ} = 0.1$ V and the set/reset voltage both in the conventional and metal NCs embedded memory cells.

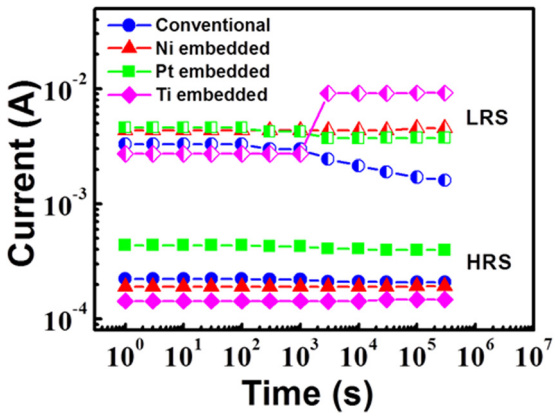

FIG. 5. Retention characteristics of the conventional and metal NCs embedded memory cells in both the HRS and LRS at a bias of 0.1 V.

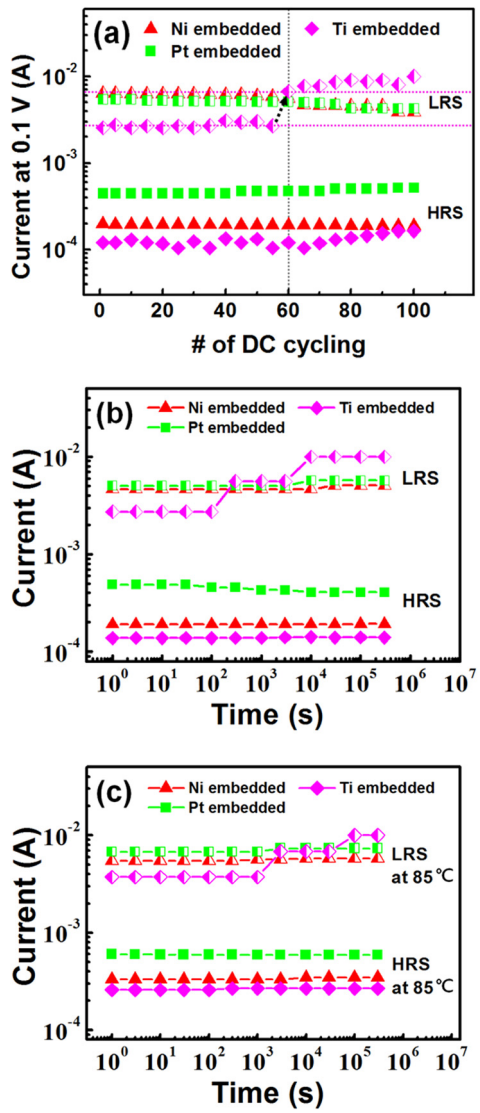

FIG. 6. (a) Endurance characteristics up to 100 cycles measured at a bias of 0.1 V for the metal NCs embedded memory cells. (b) Retention characteristics after repetitive 50 DC cycling for the metal NCs embedded memory cells at a bias of 0.1 V. (c) Retention characteristics measured at 0.1 V for the metal NCs embedded memory cells at 85 °C for 10^5 s.

LRS and HRS over 10^5 s, whereas the current ratio of Ti NCs embedded memory cells was abruptly increased after 10^3 s. Figure 6(a) shows endurance properties of the different embedded NC for repetitive 100 DC cycling, where the current at the LRS for Ti NCs embedded memory cells shows the abrupt increase in current after 60 DC cycling, while Pt and Ni NCs embedded memory cells are nearly stable at both the LRS and HRS. These results are due to the defects that occurred during the degradation of film under repetitive biases. In particular, in the Ti NCs embedded memory cells, these defects between the Ti NCs can induce additional conduction paths by connecting the densely formed Ti NCs in active layers. Therefore, the electrons can be easily transferred via the conduction paths formed by these defects (trap-based tunneling) as well as the Ti NCs, and it results in a dramatic increase of operating current. This behavior is also observed in the post endurance-retention test. We performed the retention test after repetitive 50 DC cycling for three different NC based memory cells as shown in Fig. 6(b), where we observed that the degradation is observed more quickly in Ti NC based memory cells rather than the other two memory cells. This is because the Ti NC based memory is more vulnerable to the defects induced by post-endurance test. On the other hand, Pt and Ni NC based memory devices show stable characteristics even for $>10^5$. Finally, we also measured data retention at 85 °C for different metal NCs embedded memory cells, as shown in Fig. 6(c), where overall current level of the LRS and HRS is increased due to the high leakage, caused by thermally excited electrons at high temperature.

In summary, we have demonstrated the RS characteristics of metal NCs embedded-NiN-based ReRAM cells such as Pt, Ni, and Ti. Depending on the electronegativity of metal, the size of NCs can be varied. In addition, the density of electric field near the metal NCs can be enhanced by increasing the size of NCs. The conduction mechanism can be explained differently depending on the barrier height of the potential well, formed by the difference of the work function between metal NCs and active layers. In case of Pt and Ni NCs embedded memory cells, the conduction path is formed after filling the potential wells, while in Ti embedded memory cells, the conduction path is formed by tunneling process via the Ti NCs. Therefore, we can optimize the RS properties of the ReRAM cells and predict their conduction mechanism by understanding the correlation between the embedded metal NCs and the active layers.

This work was supported by the National Research Foundation of Korea (NRF) grant funded by the Korean Government (MEST) (Nos. 2011-0028769 and 2013-044975).

[1]B. J. Choi, S. Choi, K. M. Kim, Y. C. Shin, C. S. Hwang, S. Y. Hwang, S. Cho, S. Park, and S. K. Hong, Appl. Phys. Lett. **89**, 012906 (2006).
[2]C. Y. Lin, D. Y. Lee, S. Y. Wang, C. C. Lin, and T. Y. Tseng, Surf. Coat. Technol. **203**, 628 (2008).
[3]K. Kinoshita, T. Tamura, M. Aoki, Y. Sugiyama, and H. Tanaka, Appl. Phys. Lett. **89**, 103509 (2006).
[4]S. Y. Wang, D. Y. Lee, T. Y. Tseng, and C. Y. Lin, Appl. Phys. Lett. **95**, 112904 (2009).

[5]H.-C. Tseng, T.-C. Chang, Y.-C. Wu, S.-W. Wu, J.-J. Huang, Y.-T. Chen, J.-B. Yang, T.-P. Lin, S. M. Sze, M.-J. Tsai, Y.-L. Wang, and A.-K. Chu, IEEE Electron Device Lett. **34**, 858 (2013).
[6]M. J. Lee, Y. Park, S. E. Ahn, B. S. Kang, C. B. Lee, K. H. Kim, W. X. Xianyu, and I. K. Yoo, J. Appl. Phys. **103**, 013706 (2008).
[7]Y. H. Do, J. S. Kwak, Y. C. Bae, K. Jung, H. Im, and J. P. Hong, Appl. Phys. Lett. **95**, 093507 (2009).
[8]L. Chen, H. Y. Gou, Q. Q. Sun, P. Zhou, H. L. Lu, P. F. Wang, S. J. Ding, and D. W. Zhang, IEEE Electron Device Lett. **32**, 794 (2011).
[9]W. Guan, S. Long, R. Jia, and M. Liu, Appl. Phys. Lett. **91**, 062111 (2007).
[10]C. Y. Lin, M. H. Lin, M. C. Wu, C. H. Lin, and T. Y. Tseng, IEEE Electron Device Lett. **29**, 1108 (2008).
[11]D. Y. Lee and T. Y. Tseng, J. Appl. Phys. **110**, 114117 (2011).
[12]M. C. Wu, T. H. Wu, and T. Y. Tseng, J. Appl. Phys. **111**, 014505 (2012).
[13]C. Chen, S. Gao, G. Tang, C. Song, F. Zeng, and F. Pan, IEEE Electron Device Lett. **33**, 1711 (2012).
[14]C. Y. Liu, J. J. Huang, and C. H. Lai, Thin Solid Films **529**, 107 (2013).
[15]M. J. Yun, H.-D. Kim, and T. G. Kim, J. Vac. Sci. Technol. B **31**, 060601 (2013).
[16]K. P. Ananth and L. J. Shannon, *Evaluation of Thermal Agglomeration for Fine Particle Control* (Midwest Research Institute, Washington, 2006).
[17]C. Boragno, F. Buatier de Mongeot, R. Felici, and I. K. Robinson, Phys. Rev. B **79**, 155443 (2009).
[18]I. Kim, T. S. Lee, D. S. Jeong, W. S. Lee, and K.-S. Lee, J. Phys. D: Appl. Phys. **45**, 065101 (2012).
[19]H. D. Kim, H. M. An, and T. G. Kim, IEEE Trans. Electron Devices **59**, 2302 (2012).